Adaptive optics for fluorescence wide-field microscopy using spectrally independent guide star and markers

Pierre Vermeulen
Eleonora Muro
Thomas Pons
Vincent Loriette
Alexandra Fragola

SPIE

Adaptive optics for fluorescence wide-field microscopy using spectrally independent guide star and markers

Pierre Vermeulen, Eleonora Muro, Thomas Pons, Vincent Loriette, and Alexandra Fragola
Laboratoire de Physique et d'Etude des Matériaux, École Supérieure de Physique et de Chimie Industrielles,
Centre National de la Recherche Scientifique UMR 8213, Université Pierre et Marie Curie, Université Denis Diderot,
10 rue Vauquelin, Paris 75005, France

Abstract. We describe the implementation and use of an adaptive optics loop in the imaging path of a commercial wide field microscope. We show that it is possible to maintain the optical performances of the original microscope when imaging through aberrant biological samples. The sources used for illuminating the adaptive optics loop are spectrally independent, in excitation and emission, from the sample, so they do not appear in the final image, and their use does not contribute to the sample bleaching. Results are compared with equivalent images obtained with an identical microscope devoid of adaptive optics system. © *2011 Society of Photo-Optical Instrumentation Engineers (SPIE).* [DOI: 10.1117/1.3603847]

Keywords: adaptive optics; microscopy; fluorescence; aberrations; image enhancement.

Paper 10668R received Dec. 20, 2010; revised manuscript received Apr. 5, 2011; accepted for publication Jun. 3, 2011; published online Jul. 27, 2011.

1 Introduction

Microscope objective lenses are complex optical systems that are diffraction-limited and usually have large numerical apertures. Therefore, any discrepancy between their design configuration and the one in which they are actually used can result in a dramatic degradation of the microscope optical performances. Optical microscopes are thus designed to work in a very precise and restrictive optical configuration. For example, biological objective lenses are designed to give diffraction-limited images only for the sample parts lying directly below the cover-glass, and are optimized to work with a given cover-glass thickness. Imaging through thick samples usually leads to poor quality results because microscope objective designs cannot take into account sample induced aberrations. One possibility to get rid of this limitation is to add an extra correction in the imaging path of the microscope in order to correct aberrations introduced by the sample itself, and by the optical components added to implement this aberration correction system.

The classical implementation of an aberration correction system, initially developed for astronomy, is based on the use of an adaptive optics (AO) loop. This loop is made of a wave-front modulating device like a deformable mirror (DM) or a spatial light modulator, coupled to an acquisition device providing a correction criterion like a Shack–Hartman (S–H) wave-front sensor or a detector working with a dedicated signal processing software.

As emphasized by Booth,[1] the use of a S–H to measure distorted wave-fronts is not trivial in microscopy as it requires a point source emitter which is not naturally present in samples. Therefore, most of the AO loop described in the past few years have proposed different strategies to circumvent the problem of wave-front measurements.

The first possibility is to compute the aberrations induced by the optical index mismatch, or the optical design.[2–4] This technique is efficient when low-order aberrations are important but fails to take into account the specific aberrations induced by the samples.

In point by point techniques (confocal, two-photon microscopy) the focusing of the excitation beam generally ensures that the maximum signal is collected when aberrations are minimal. An optimization algorithm is then sufficient to find the ideal shape of the deformable mirror. This optimization can be performed point by point [5–7] or on the total image intensity.[8,9] In multiharmonic microscopy, due to the complex interaction inside the sample, the previous assumption can be inexact, as shown by Ref. 10. However, the use of the image sharpness remains a satisfactory criterion for correction in third harmonic microscopy.

In wide-field microscopy, Débarre and colleagues have developed, a specific algorithm to extract a metric from the images, which can provide a correction criterion for the AO loop.[11,12]

To determine the optimal correction, these techniques use either hill-climbing algorithms, genetic algorithms, or the addition of known aberration bias, which require a large amount of images and an increase of the exposure time. This is the major limitation when observing fluorescent samples inclined to photobleach. Moreover, if the initial aberrations are important, an algorithm can get stuck in local minima of the search space, and provides nonoptimal correction.

On the other hand, direct measurement of the wave-front allows fast and accurate correction which can protect the sample from photobleaching. Wave-fronts can be measured with an interferometer using the scattered illumination light,[13,14] or using a Shack–Hartman sensor, which requires the use of point source emitters, usually small beads inside the samples. An advantage of using a S–H is that the beads size is not limited by the objectives NA so large beads can be used, typically a few micrometers

in diameter. Those "guide stars" or "beacons" allow collection of strong signals, thus providing fast wavefront measurements with high signal-to-noise ratio.[15, 16]

In Ref. [17], plastic beads focus illumination light inside the sample and generate stars used to improve the precision and strength of optical tweezers.

Recently, Azucena et al.[18] have successfully demonstrated the ability of a S–H/DM loop to measure and correct the wavefront from fluorescent beacons injected in a drosophila embryo.

For this wave-front correction to result in an improvement of the sample image quality, additional criteria must be fulfilled:

- the imaging and wavefront measurement optical paths should exhibit the same aberrations, or the aberration difference must be measured and compensated for;
- the star illumination must not photobleach the fluorophores of the sample while the AO loop is running. This can be achieved either by localizing the guide star illumination,[18] or by using different excitation bands for the star and the sample.

The use of bright guide stars to improve the speed and accuracy of wave-front measurements can pollute the fluorescence image and hide sample small features, so we opt for stars having an emission spectrum different from the sample.

In this article we describe a wide-field fluorescent microscope based on these principles, where aberrations induced by the sample are corrected with an adaptive loop using extra fluorescent guide stars physically and spectrally independent of the sample. In Sec. 2 we describe the optical setup inserted between a commercial microscope and an imaging CCD camera.

In Sec. 3 the system performances are described and compared to the same microscope working without an AO loop. Sample measurements on biological samples are shown in Sec. 4.

2 Measurement Principle and Set-up

The working principle of our setup is the following: the adaptive optics loop uses a single fluorescent bead as a guide star. This bead is placed close to the center of the microscope field of view and has an emission spectrum centered around 620 nm. The AO loop field of view is reduced down to approximately 10% the full field of view in order to eliminate the signal coming from other fluorescent beads that may be present in the neighborhood of the guide star. The sample is tagged with another fluorescent marker with an emission spectrum centered at 550 nm. A dichroic filter in the optical setup directs the 620 nm signal on the wave-front sensor, and the 550 nm signal on a CCD camera, so the guide stars are not seen by the camera while the sample fluorescence does not pollute the guide star signal on the wave-front sensor. This allows us to obtain science images devoid of spurious star images, clean star signals on the S–H and use of very bright stars. It also permits us to measure wave-fronts using an uncooled S–H camera with the integration times of the order of 100 ms. If the wavelengths are not properly chosen, the large wavelength difference between the guide star and the sample could reduce the system ability to compensate chromatic aberrations. Here it is not a severe limitation because the achromatic doublets used in our setup are corrected for C and F lines that are close to the chosen wavelengths. Ray-tracing simulations of our system show that the lateral chromatic aberration (lateral color) is 6 μm
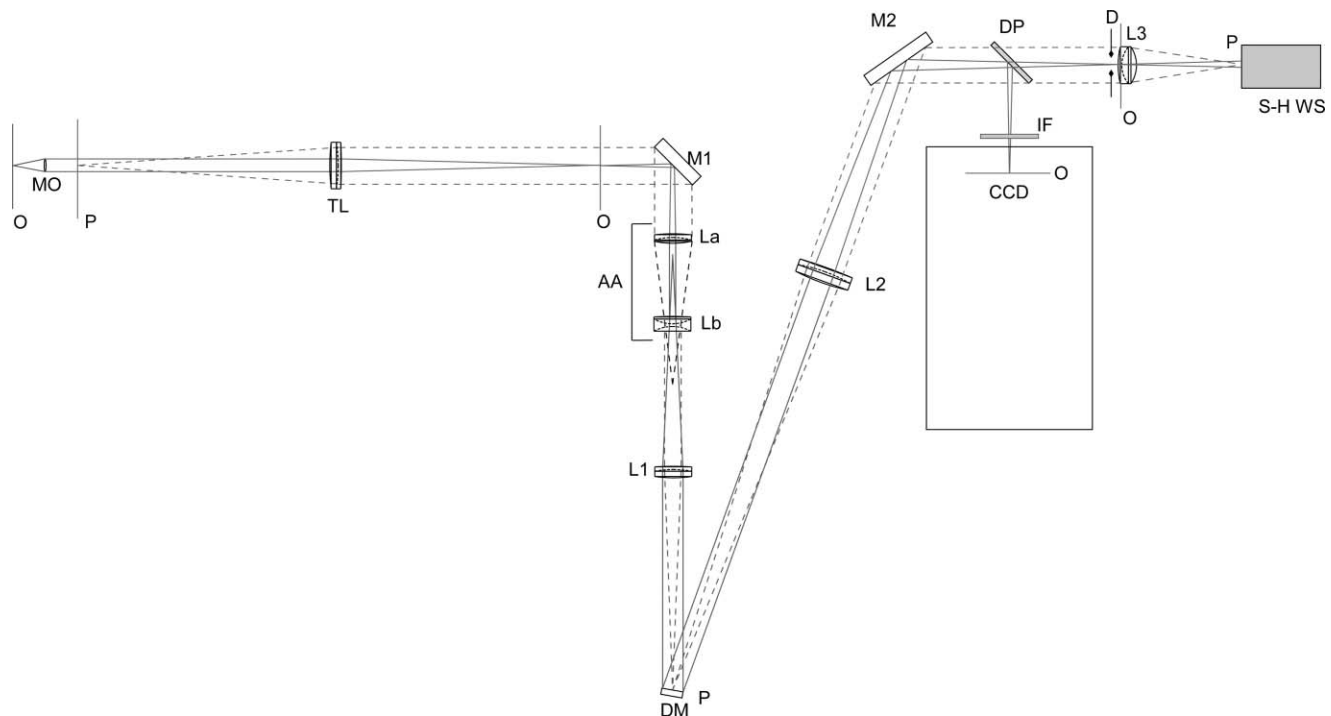
Fig. 1 Scheme of the setup. The microscope body is not shown. O: object and conjugate planes; MO: microscope objective; P: objective exit pupil and conjugate planes; TL: microscope tube lens; M1, M2: silver coated flat mirrors; La, Lb afocal attachment ($f_A = +100$ mm, $f_B = -40$ mm), L1: lens ($f_1 = +150$ mm), L2: imaging lens ($f_2 = +300$ mm); DP: dichroic plate; CCD: science camera; IF: interference filter; D: iris diaphragm; L3: lens ($f_3 = +70$ mm), S–H: Shack–Hartman wave-front sensor. All lenses are 1 in. diameter achromatic doublets except L2 which is a 40 mm diameter achromat.

at the edge of the field of view, which is smaller than our camera pixel size, and the chromatic focal shift is 50 μm at the focus of a $f = 300$ mm imaging lens.

Using well separated excitation wavelengths allows us to avoid photobleaching of the sample while exciting the stars during the time needed by the loop to reach the best wave-front correction.

The setup presented in Fig. 1 was designed to fit the camera output port of a commercial microscope body.

We worked on a Olympus IX71 inverted microscope. The DM (Imagine Optic, Mirao e52) is placed in a plane conjugate to the microscope objective exit pupil. It is slightly tilted with respect to this plane. The mirror diameter is $D_{DM} = 15$ mm. The focusing lens that images the pupil on the DM is preceded by an afocal attachment. The role of this telescope is to reduce the overall dimensions of the setup, but it may be used also in combination with the focusing lens as a variable power zoom system to adapt the magnification between the objective exit pupil and the deformable mirror. The configuration shown here was designed for the $60\times$, NA $= 1.2$ water immersion objective that was used for all the presented results. It must be noted, however, that the presence of this three-lens system inevitably reduces the optical quality of the imaging setup and adds extra wave-front deformation. The CCD camera (Roper Quantem 512) is placed in a plane conjugate to the sample thanks to an imaging lens, 40 mm in diameter, having roughly the same focal length $f = 300$ mm as the three-lens system. This insures a magnification factor close to 1, in practice 0.788, between the intermediate image plane and the camera. The micro-lens array of the Shack–Hartman sensor (Imagine Optic, Haso3 first) is placed in a plane conjugate to the deformable mirror. In order to control independently the imaging camera field of view and the detector field of view, an iris diaphragm is placed close to the lens in front of the microlens array. Imaging and wave-front control paths are split by a thin dichroic plate (Semrock). The lenses positions are adjusted sequentially using a source at infinity made of a $\lambda = 550$ nm light-emitting diode illuminating a pinhole placed in the focal plane of a $f = 100$ mm achromat. The source is aligned prior to the setup using a Shack–Hartman sensor. With this tool, each lens position can be adjusted to within 1 mm from its optimal position.

This optical design fulfills as much as possible the requirement of aberration equality between the S–H path and the imaging path. Three components may generate unbalanced aberrations: the dichroic plate, the lens in front of the S–H, and an optional filter placed in front of the camera. The most critical element is the dichroic filter. Aberrations generated by this component cannot be cancelled by the loop, unless they are evaluated prior to the measurement, and this information is sent to the DM as an extra deformation. We measured the transmitted and reflected wave-front deformation on a 3.6-mm diameter surface, sampled by 32×32 microlenses, by placing the plate between a wave-front analyzer and a source at infinity, previously adjusted with the S–H. The plate was tilted by $45°$ and held by the same plate holder as in the setup. Figures 2(a) and 2(b) show the wave-front deformation added by the presence of this plate.

From this measurement we conclude that the presence of the plate should limit the system performances to a Strehl ratio of 0.98 (a definition of the Strehl ratio is given in Sec. 3). This result is surprisingly good as the plate was not specifically designed
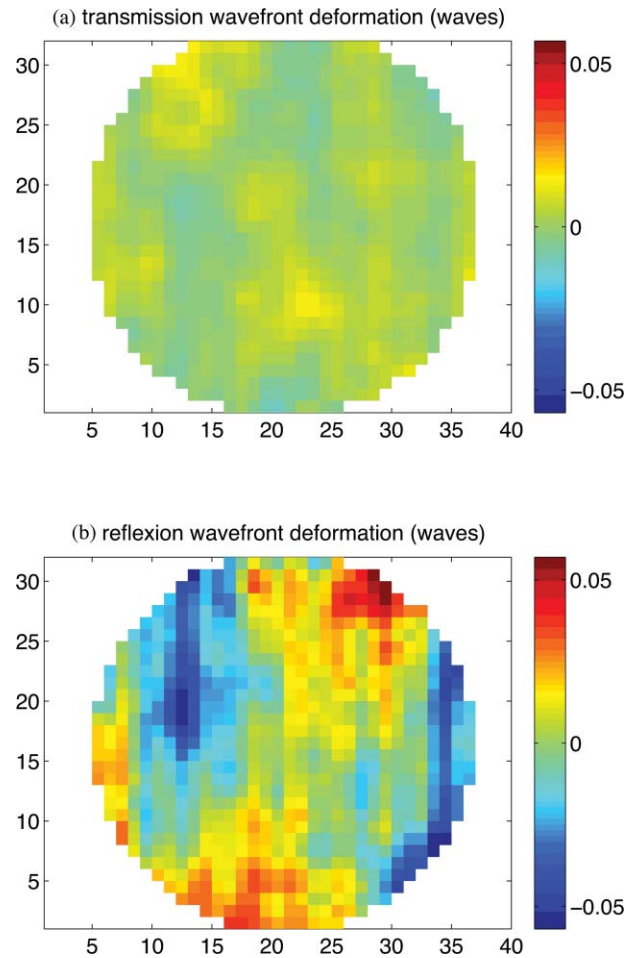
Fig. 2 Wavefront deformations induced by the dichroic plate, expressed in waves. (a) Transmission map. (b) Reflection map.

to provide low reflected wave-front distortion. A similar wave-front measurement was done on the interference filter. In order to cancel the aberrations induced by the lens in front of the S–H, and by the interference filter, both components should ideally be placed in planes conjugate to the sample. Although this is done in the case of the lens, the filter cannot be placed exactly on the image plane for practical reasons as well as in order to avoid imaging the filter surface on the camera. The distance between the filter and the CCD array is $d = 1$ cm. Aberrations induced by this component that could degrade the image quality would arise from sections of $D_{DM} \times D/f \approx 0.5$ mm in diameter. We measured the wave-front deformations induced by the filter and found an rms deformation of 4 nm, which corresponds to a Strehl ratio higher than 0.99.

The guide stars are quantum dots (QDs) labeled beads. CdSe/CdS/ZnS hydrophobic multishell QDs were prepared following the SILAR protocol and purified by precipitation in ethanol and re-suspension in chloroform.[19] Typically, 6 nmol of QDs emitting at 620 nm were mixed with 200 mg polystyrene in 4 ml chloroform. This solution was mixed with a 15 ml aqueous solution (7 g/l sodium dodecylsulfate, 0.1 M sodium bicarbonate), and vortexed using an Ultraturrax homogenizer. The solution was then stirred for 24 h in an open vial to evaporate the chloroform.

3 Characterization of the Imaging System

3.1 Performances with Water-Immersed Fluorophores

The ability of our AO loop working with red emitting stars to efficiently improve the CCD image is not obvious. In order to check it and evaluate the performances of our system for correcting the wave-front reflected by the dichroic plate we must evaluate the Strehl ratio, not from the S–H signal, as this would only give information on the loop performances, but directly from the science image. We used the Strehl ratio S as an indicator of the system performances and ability to maintain or improve the images quality. It is defined as the peak intensity of a point emitter aberrated image, divided by the peak intensity of a point emitter unaberrated image, both images having the same total intensity. For direct imaging of subresolution point sources for Strehl estimation, it has been shown that careful choice of the algorithm and ratio of pixel size to Airy disk radius are important for accuracy.[20] To improve our measurement of the Strehl ratio, we used a CCD with 6.45×6.45 μm^2 pixels (Pixelfly), and the Airy disk radius on the camera, while using a $\times 60$ water immersion objective at 510 nm, is 13 μm, so the point spread function(PSF) spreads over a dozen pixels.

First, we corrected 50 aberration modes using a guide star close to the center of the microscope field of view. The corrected

modes are the eigenvectors of the interaction matrix measured by the AO loop. They form an orthonormal basis, but their shape depends on the optical setup geometry, in particular the pupil shape and number of microlenses. They have to be distinguished from the Zernike modes usually used to represent wavefront aberrations. However, these corrected modes can be projected on a Zernike function basis, and the aberrations measurements presented in this paper are decomposed on this familiar Zernike basis. Then we took a CCD image of a field containing randomly distributed 200 nm diameter beads localized in the plane of the guide star [see Fig. 3(a)].

We evaluated the Strehl ratio of individual beads: we measured, for each bead image, the fraction of the total signal present in the brightest pixel. The results were then corrected to take into account the beads diameter, pixel size, magnification factor, and the distance between the beads images barycenter and the corresponding brightest pixel center. Figure 3(b) shows a map of the measured Strehl ratio across the science image. From these results we were able to calculate the Strehl ratio as a function of the distance to the guide star that was close to the image center, as shown in Fig. 3(c). The Strehl ratio evaluated this way gives a value of $S_{\mathrm{CCD}} = 0.959 \pm 0.039$ when using the four beads closest to the guide star position. The behavior of the Strehl ratio with the distance to the guide star depends on the number of corrected modes. We performed the same calculations with
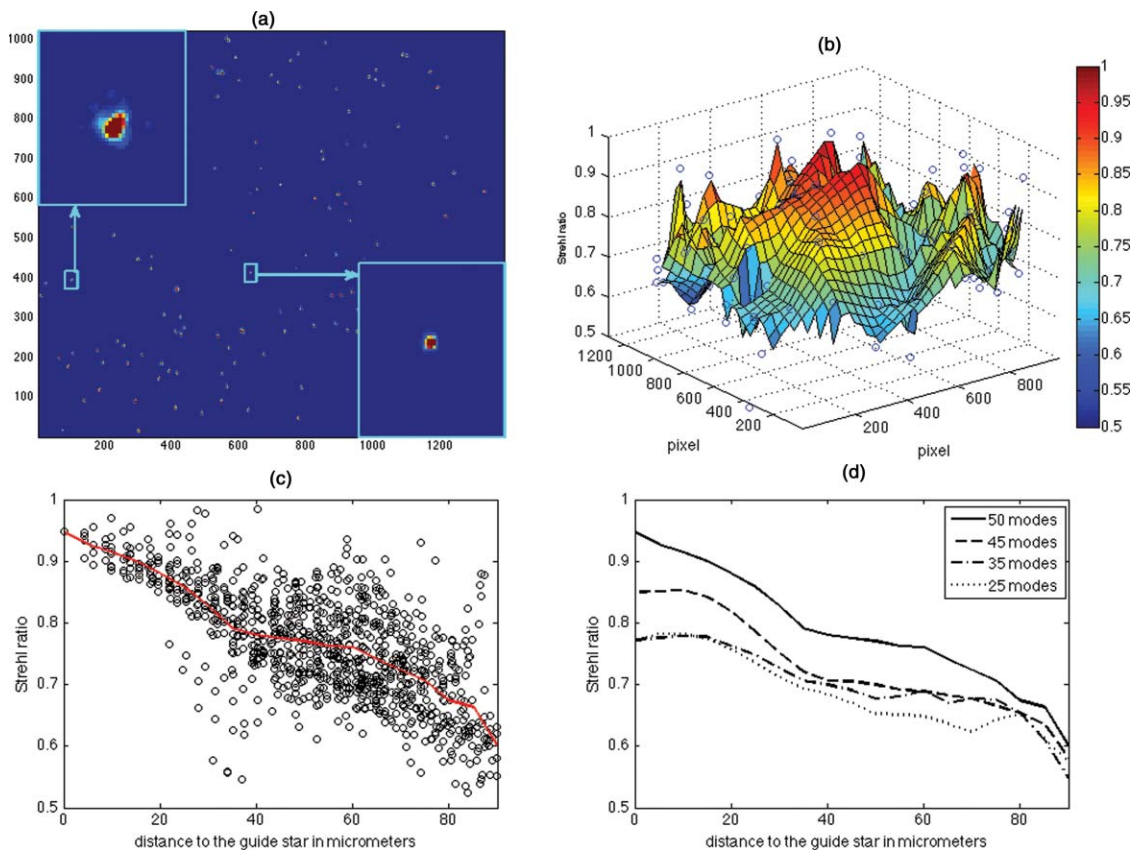
Fig. 3 Strehl ratio improvement plot over the whole camera field of view. a: 136 μm$\times$177 μm raw science image. The two insets show the images of two 200-nm diameter beads at $\approx$ 10 μm and $\approx$ 50 μm from the guide star. (b): Strehl ratio map calculated with the raw image. (c) Strehl ratio as a function of the distance to the guide star the "∘" show individual measurements, and the red line is an average plot. (d) Strehl ratio as a function of the distance to the guide star for different numbers of corrected aberration modes. The graphs were computed using 140 evenly distributed fluorescent beads in water, using the CCD data. The maximum Strehl ratio calculated using the image data is 0.959.

different corrections. The result is presented in Fig. 3(d). The plots differ by the order of the highest corrected mode. The common value of the Strehl ratio at the edge of the image proves that the higher the order number, the smallest its correlation length, so the smallest its influence far from the guide star. On the contrary, close to the guide star, the image quality improvement strongly depends on the number of corrected modes.

The Strehl ratio can also be estimated from the wave-front sensor data, [15] using the standard approximation:

$$S \approx \exp\left(-\left[2\pi\sigma_w\right]^2\right), \qquad (1)$$

where σ_w is the wave-front standard deviation expressed in waves measured by the Shack–Hartman sensor. This formula works well for Strehl ratios higher than 0.1. We compared this estimation to the previous measurements performed on the point source images. The wave-front standard deviation measured during the acquisition for the previous image was 0.033λ using the guide star signal, so the Strehl ratios is $S_{\text{S–H}} = 0.957$. The good agreement between both estimates demonstrates the ability of our algorithm to accurately estimate Strehl ratio of subresolution particles, despite the weak number of pixels for each PSF. This result shows that the residual wavefront aberrations are very close in the S–H signal and in the CCD arm, so the AO loop can successfully improve the quality of the CCD image.

However, it is important to note that a commercial microscope is usually very well corrected, so Strehl ratios higher that 0.8, up to 0.9, are usually expected when imaging aberration-free samples. When we set the DM to a flat shape, the Strehl ratio measured with the S–H drops below 0.3. This result shows that the image quality is degraded mostly by the extra optical setup and misalignment of its optical components. We found that the dominant aberrations of our setup were astigmatism and coma. The AO loop must thus be used anytime to maintain the original microscope Strehl ratio, even when no sample-induced aberration is present. However, as the correction of the setup induced aberrations does not use more than a quarter of the deformable mirror stroke, it is not a severe limitation.

3.2 Surface of Preserved Performances

The optical performances of the original microscope cannot be preserved across the full field of view [see Figs. 3(c) and 3(d)], because the AO loop can only correct the wave-front from one single star at a given time. Figure 3(d) allows us to give a rough estimate of the surface surrounding the beacon where the Marechal criterion $S > 0.8$ is satisfied, and where we can expect the loop to preserve the microscope optical performances. 30 μm away from the guide star, the Strehl ratio falls below 0.8. Outside this region, the presence of the extra optical setup deteriorates the performances of the microscope. However, when imaging samples with aberrations, it helps to maintain the Strehl ratio to a given value. At the edge of the field of view the Strehl ratio stays larger than 0.6. This is, of course, the case only if the aberrations are constant throughout the field of view. As a comparison, a very good plan-apochromatic objective keeps a Strehl ratio higher than 0.8 up to 85% of the field diameter,[21] while in our case it is roughly 30% of the field diameter.
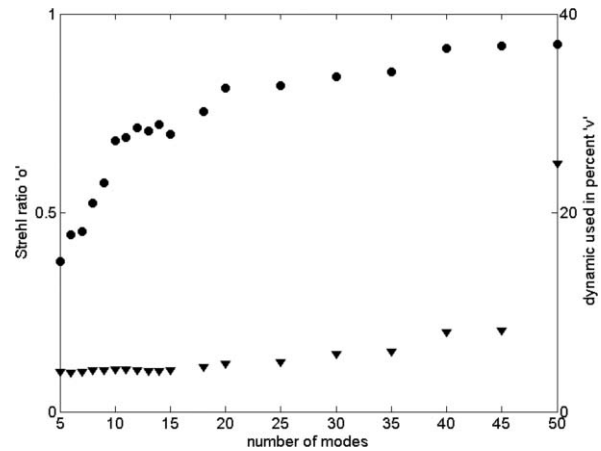

Fig. 4 Strehl ratio (bullet) and DM used displacement range (triangle) as a function of the number of corrected modes

3.3 Performances Versus Number of Corrected Modes

The time needed to compute the AO loop correction matrix is a quadratic function of the number of corrected modes, and the amount of DM displacement used increases with the number of corrected modes. It is important to find the minimum number of corrected modes that will allow to obtain a given Strehl ratio.

The image quality improvement, close to the guide star, as a function of the number of corrected modes n is presented in Fig. 4. The sample was made of a fluorescent beacon in water. When 50 modes are corrected, the Strehl ratio is 0.92 and is higher than 0.8 as soon as $n > 20$. It is important to notice that the displacement of the most solicited actuator stays below 7% of the DM stroke except when 50 modes are corrected, in which case 23% of the displacement range is used.

4 Results

4.1 Consistency of the Measured Aberrations Magnitude

The consistency between the measured aberration amplitudes and the sample induced aberrations was tested by using a stack of two 170-μm thick cover-glasses instead of a single cover-glass. We looked at a guide star directly below the cover-glasses. In this case the uncorrected image was so poor that we found it impossible to evaluate the Strehl ratio. We used this measurement to check the consistency between the measured Zernike amplitudes and the calculated ones. We first checked that our optical setup was free of spherical in the absence of the extra cover-glass. The presence of the extra cover-glass induces an amount of longitudinal spherical LA_M equal to:[22]

$$LA_M = \frac{t}{n}\left(1 - \frac{n\cos[U]}{\sqrt{n^2 - \sin^2[U]}}\right), \qquad (2)$$

where n is the refraction index of the cover-glass divided by the water refraction index, t is the cover-glass thickness, and U is the slope angle of the marginal ray. The peak wavefront error OPD_{max} associated with the third order spherical when the

aberration rms error is minimized, is

$$\text{OPD}_{\text{max}} = \frac{LA_M}{16} n_{\text{water}} \sin^2 [U] \,, \qquad (3)$$

and the corresponding Zernike standard deviation is[23]

$$\sigma_{\text{OPD}} = 0.0745 \times \text{OPD}_{\text{max}}. \qquad (4)$$

The value calculated using Eqs. (2)–(4) is $\sigma_{\text{OPD,calc.}}$ = 0.316 μm, the measured value is $\sigma_{\text{OPD,meas.}}$ = 0.341 μm. This result, although very partial, makes us confident in the possibility to accurately measure the amount of aberrations induced by samples, assuming we have a precise prior measurement of the setup induced aberrations.

4.2 Comparison with a Standard Microscope with Aberrant Samples

We first checked that our AO loop is able to preserve the performances of a microscope when imaging aberrant samples. The absolute performances of our setup were judged by comparing them with the performances of an identical microscope devoid of adaptive optics loop. We used the same camera, microscope objective, and filter cube in an identical microscope body. When testing a sample made of beads placed directly on the coverslip and correcting 20 modes, we found that the loop did not bring any significant improvement, which simply confirms the good optical quality of our microscopes with $S > 0.8$. We then used a second sample made of fluorescent guide stars immersed 75 μm deep inside a thick 10% agarose solution. As we work with an inverted microscope, the agarose solution lies between the star and the microscope objective. The standard microscope gave $S \approx 0.3$. The modified microscope also gave $S = 0.3$ when we applied the 20 mode correction obtained with the first sample, thus correcting only the setup induced aberrations. A Strehl of 0.82 was measured with the adaptive optics loop correcting also the sample-induced aberrations 20 first modes. The DM displacement used in this case was 7%. This result shows that the loop preserves the original optical performances of our microscope by correcting 20 modes when imaging through moderately aberrant samples.

4.3 Cells

HeLa cells, grown in Dulbecco's Modified Eagle Medium (DMEM) medium supplemented with 10% Fetal Bovine Serum (FBM) and 1% antibiotics, were deposited on poly-allylamine-treated coverslips to promote the adherence of QD beads. After 24 h cells were fixed 20 min in 2% formaldehyde, rinsed 3 times in phosphate buffered saline (PBS), and permeabilized 5 min in 0.5% triton. After 5 rinsings in PBS, cells were incubated 1 h with the primary antibody diluted to 0.5 mg/ml in PBS (anti β-tubulin, Cytoskeleton), and then washed 3 times in PBS. Then cells were incubated 1 h with the secondary antibody diluted to 8 g/ml in PBS (antimouse- Alexa488, Invitrogen) and afterwards rinsed 3 times in PBS. Finally cells were incubated with QD beads for 1 h and then directly mounted on a slide with Mowiol 4-88.

We recorded images of the cells using the same protocol as above, but correcting 50 modes instead of 20. The AO loop was first run to correct the setup aberrations using an isolated
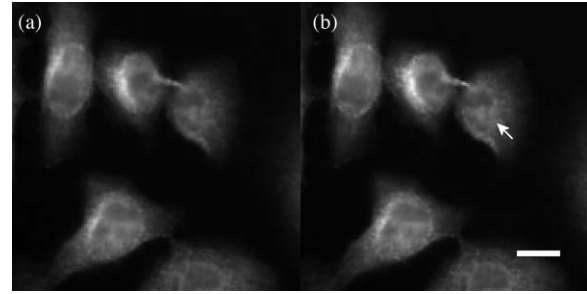

Fig. 5 Images of tubulin stained Hela cells. (a) The DM shape was set to correct only setup aberrations, (b) The AO loop corrected all aberrations, including sample induced aberrations. The bar length is 10 mm. The guide star is not visible in the images, its position is indicated by the arrow.

guide star. The obtained Strehl ratio, estimated using the residual wavefront data, was $S = 0.987 \pm 0.004$ and the used DM stroke 20%. The sample was then moved until a guide star was found above a cell. This cell was thus between a guide star and the microscope objective. At this position the Strehl ratio decreased to $S = 0.73 \pm 0.03$. The loop was then used to recover the initial Strehl. We obtain $S = 0.985 \pm 0.002$ with 34% used dispalcement of the DM. Figure 5 illustrates this point. Figure 5(a) was taken with the loop correcting the setup induced aberrations. Figure 5(b) was taken with the loop running so as to correct all the aberrations, including the ones induced by the cell. The rms wavefront error is 70 ± 5 nm in the first image, and 12 ± 1 nm in the second one. The improvement appears more clearly in Fig. 6 which shows the spatial frequency spectra of the two images. The increase of high frequency content is clearly visible, but unluckily a gain in cutoff frequency does not appear because of the limited sampling of our optical system. The wave-front maps presented in Fig. 7 correspond to the same data set. The residual wave-front [Fig. 7(a)] is induced by the presence of the cell between the star and the microscope. It is balanced by the AO loop as can be seen in wave-front
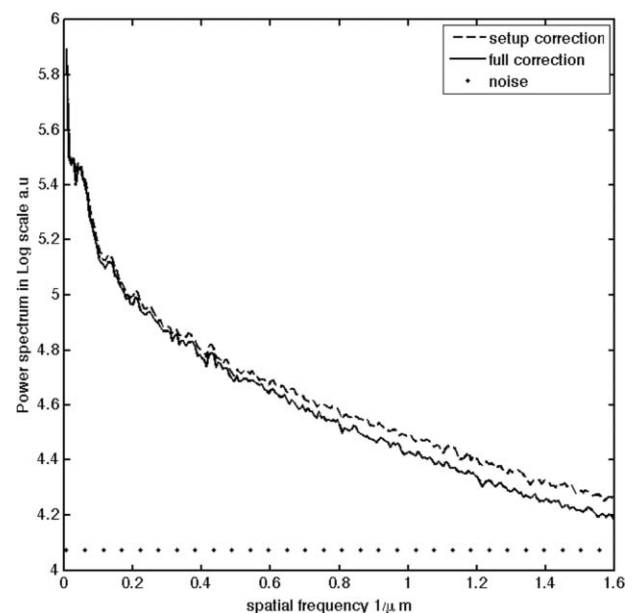
Fig. 6 Spatial frequency spectra of the two images in Fig. 5
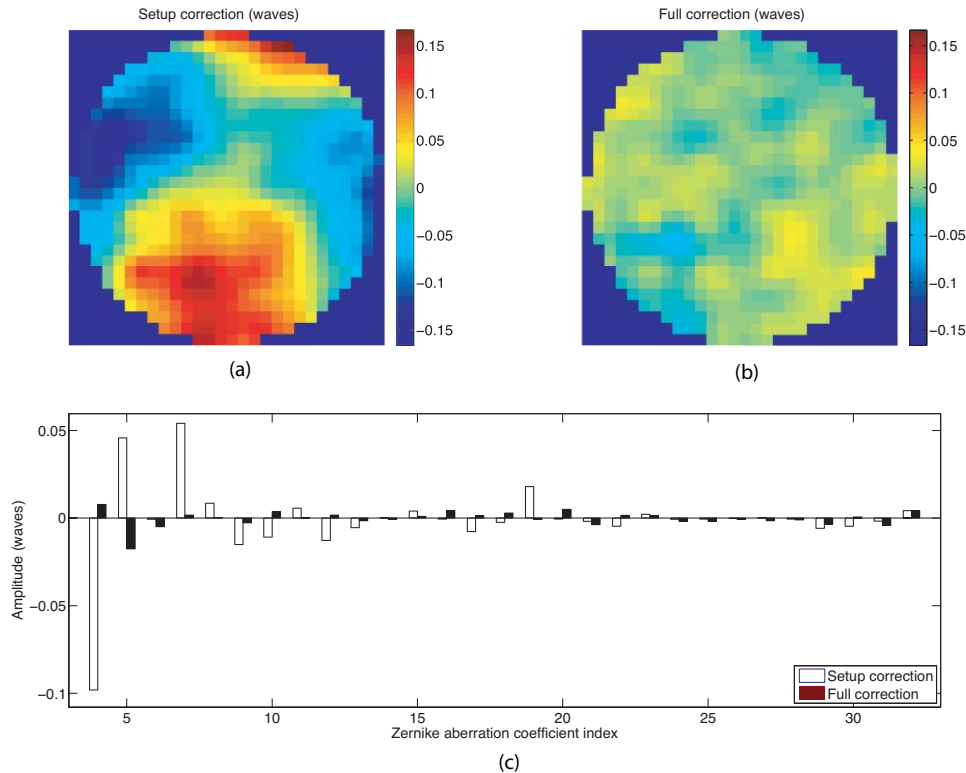
Fig. 7 Wave-front maps and amplitudes of the first 32 Zernike coefficients expressed in waves corresponding to the measurements shown in Fig. 5. (a) Wave-front map recorder with the DM shape set to correct the optical setup aberrations. (b) Same wave-front recorded with the AO loop correcting all aberrations. (c) Comparison of the aberration coefficients (focus shift and tilt aberrations are not present in this histogram).

[Fig. 7(b)]. The aberration decomposition on a Zernike basis of the two wave-fronts is show in [Fig. 7(c)].

5 Discussion and Prospects

Implementation of an adaptive loop in the imaging path of a standard wide-field fluorescence microscope has been presented. The use of an adaptive optics technique, combined with the introduction of fluorescent guide stars into the sample, allows to preserve the imaging performances of the original microscope when observing aberrant samples like stained cells. Observation of cells with the adaptive optics loop setup to correct the aberrations induced by the sample requires 34% of the mirror stroke.

The main advantage of using red stars when observing green stained samples is that the stars do not appear in the cell images and do not mask regions of interest in the sample. They can be made very bright. Although the wavelength difference between the measurement and the imaging signals does not allow an optimal correction of the sample induced aberrations in the fluorescence image, it permits to improve the image quality as demonstrated above.

Moreover, using stars made of red or near-infrared emitting wavelength fluorophores preserves the sample from photobleaching while measuring the wave-front and calculating the best shape of the deformable mirror: guide stars can be strongly excited with a specific source that is not absorbed by the sample. The fluorophores tagging the sample are illuminated only for final and corrected image acquisition.

As the addition of guide stars into the sample and the implementation of an adaptive loop in the imaging path are com-pletely independent of the illumination path of the microscope, this setup can be easily combined with wide field structured illumination techniques like grid or fringe projection microscopy.

The current limitations of this setup are:

- the modest size of the corrected field of view compared to the microscope full field of view. If the dynamic aspect of the measurement is crucial, multiconjugate adaptive optics may significantly improve the size of the isoplanetic patches.[24] In the case of static measurements, sequential corrections performed using guide stars uniformly distributed within the sample can be used to synthesize a fully corrected image.
- the inability to correct the aberrations at all depths in thick samples. This limitation is inherent to all wavefront correction systems, but could eventually be partially circumvented by measuring the aberrations using stars behind the sample and in front of it. The aberration differences being induced by the sample itself, a linear interpolation of the aberrations amplitude could enhance to first order the images quality at any depth, provided the aberrant regions are distributed homogeneously within the sample.
- the current inability to control the guide star position and place it at a chosen location close to a region of interest. This point would require further work on the sample preparation and would certainly be sample dependent.

References

1. M. J. Booth, "Adaptive optics in microscopy," *Philos. Trans. R. Soc. London, Ser. A* **365**, 2829–2843 (2007).
2. P. Kner, J. W. Sedat, D. A. Agard, and Z. Kam, "High-resolution wide-field microscopy with adaptive optics for spherical aberration correction and motionless focusing," *J. Microsc.* **34**, 136–147 (2009).
3. B. Potsaid, Y. Bellouard, and J. T. Wen, "Adaptive scanning optical microscope (asom): A multidisciplinary optical microscope design for large field of view and high resolution imaging," *Opt. Express* **13**(17), 6504–6518 (2005).
4. Z. Kam, P. Kner, D. Agard, and J. W. Sedat, "Modelling the application of adaptive optics to wide-field microscope live imaging," *J. Microsco.* **226**(1), 33–42 (2007).
5. A. J. Wright, S. P. Poland, J. M. Girkin, C. W. Freudiger, C. L. Evans, and X. S. Xie, "Adaptive optics for enhanced signal in cars microscopy," *Opt Express* **15**, 18209–18219 (2007).
6. L. Sherman, J. Y. Ye, O. Albert, and T. B. Norris, "Adaptive correction of depth-induced aberrations in multiphoton scanning microscopy using a deformable mirror," *J. Microsc.* **206**, 65–71 (2002).
7. N. Ji, D. E. Milkie, and E. Betzig, "Adaptive optics via pupil segmentation for high-resolution imaging in biological tissues," *Nat. Methods* **7**, 141–147 (2010).
8. D. Debarre, E. J. Botcherby, T. Watanabe, S. Srinivas, M. J. Booth, and T. Wilson, "Image-based adaptive optics for two-photon microscopy," *Opt. Lett.* **237**, 2495–2497 (2009).
9. M. J. Booth, M. A. A. Neil, R. Juskaitis, and T. Wilson, "Adaptive aberration correction in a confocal microscope," *Proc. Natl. Acad. Sci. U.S.A.* **99**(9), 5788–5792 (2002).
10. N. Olivier, D. Débarre, and E. Beaurepaire, "Dynamic aberration correction for multiharmonic microscopy," *Opt. Lett.* **34**, 3145–3147 (2009).
11. D. Debarre, M. J. Booth, and T. Wilson, "Image based adaptive optics through optimisation of low spatial frequencies," *Opt. Express* **15**, 8176–8190 (2007).
12. D. Debarre, E. J. Botcherby, M. J. Booth, and T. Wilson, "Adaptive optics for structured illumination microscopy," *Opt. Express* **16**, 9290–9305 (2008).
13. M. Feierabend, M. Ruckel, and W. Denk, "Coherence-gated wave-front sensing in strongly scattering samples," *Opt. Lett.* **29**(19), 2255–2257 (2004).
14. M. Rueckel, J. A. Mack-Bucher, and W. Denk, "Adaptive wavefront correction in two-photon microscopy using coherence-gated wavefront sensing," *Proc. Natl. Acad. Sci. U.S.A.* **103**(46), 17137–17142 (2006).
15. J. L. Beverage, R. V. Shack, and M. R. Descour, "Measurement of the three-dimensional microscope point spread function using a shack-hartmann wavefront sensor," *J. Micros.* **205**, 61–75 (2002).
16. M. Oberlaender, P. J. Broser, B. Sakmann, and S. Hippler, "Shack-Hartmann wave front measurements in cortical tissue for deconvolution of large three-dimensional mosaic transmitted light brightfield micrographs," *J. Micros.* **233**(2), 275–289 (2009).
17. M. Reicherter, W. Gorski, T. Haist, and W. Osten, "Dynamic correction of aberrations in microscopic imaging systems using an artificial point source," *Proc. SPIE* **5462**, 68–78 (2004).
18. O. Azucena, J. Crest, J. A. Cao, W. Sullivan, P. Kner, D. Gavel, D. Dillon, S. Olivier, and J. Kubby, "Wavefront aberration measurements and corrections through thick tissue using fluorescent microsphere reference beacons," *Opt. Express* **18**, 17521–17532 (2010).
19. R. Xie, U. Kolb, J. Li, T. Basché, and A. Mews, "Synthesis and characterization of highly luminescent CdSe-core CdS/$Zn_{0.5}Cd_{0.5}$S/ZnS multishell nanocrystals," *J. Am. Chem. Soc.* **127**, 7480–7488 (2005).
20. L. C. Roberts, Jr., M. D. Perrin, F. Marchis, A. Sivaramakrishnan, R. B. Makidon, J. C. Christou, B. A. Macintosh, L. A. Poyneer, M. A. van Dam, and M. Troy, "Is that really your strehl ratio?" in "*Society of Photo-Optical Instrumentation Engineers (SPIE) Conference Series,*" Vol. 5490 Presented at the Society of Photo-Optical Instrumentation Engineers (SPIE) Conference, R. R. D. Bonaccini Calia and B. L. Ellerbroek, Eds., pp. 504–515 (2004).
21. H. Gross, F. Blechinger, and B. Achtner, *Handbook of Optical Systems*, Vol. 4, p. 564, Wiley-VCH, Weinheim (2008).
22. W. J. Smith, *Modern Optical Engineering*, 4th ed., p. 35 McGraw-Hill, Ney York (2008).
23. H. Gross, F. Blechinger, and B. Achtner, *Handbook of Optical Systems*, Vol. 3 Wiley-VCH, Weinheim (2008).
24. J. Thaung, P. Knutsson, Z. Popovic, and M. Owner-Petersen, "Dual-conjugate adaptive optics for wide-field high-resolution retinal imaging," *Opt. Express* **17**(6), 4454–4467 (2009).